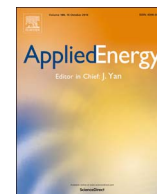




Contents lists available at ScienceDirect

Applied Energy

journal homepage: www.elsevier.com/locate/apenergy

Preparation of novel copper-powder-sintered frame/paraffin form-stable phase change materials with extremely high thermal conductivity

Zongtao Li^{a,c}, Yuxuan Wu^a, Baoshan Zhuang^a, Xuezhi Zhao^a, Yong Tang^a, Xinrui Ding^{a,b,*}, Kaihang Chen^a

^a Key Laboratory of Surface Functional Structure Manufacturing of Guangdong High Education Institutes, South China University of Technology, Guangdong, China

^b Department of Mechanical Engineering, University of California at Berkeley, CA, United States

^c Research and Development Center, Foshan, Nationstar Optoelectronics Co., Ltd, Guangdong, China

HIGHLIGHTS

- Phase change materials often exhibit high leakage and low thermal conductivity.
- Copper powder sintered frame/paraffin form-stable phase change material is prepared.
- The produced composite possesses high thermal conductivity and latent heat.
- An efficient heat sink for high power density light-emitting diodes is fabricated.

ARTICLE INFO

Keywords:

Form-stable phase change material
Copper-powder-sintered frame
Thermal management
Electronics

ABSTRACT

Owing to their high latent heat and chemical stability, phase change materials (PCMs) are often utilized for cooling high-power-density electronics. However, the application of PCMs is limited by their leakage and low thermal conductivity. In order to resolve this issue, a copper-powder-sintered frame/paraffin form-stable phase change material (CPSF/P-FSPCM) was prepared by embedding paraffin into CPSF using a vacuum perfusion method, and the dependences of its filling rate on the material porosity and CPSF thickness were determined. In addition, transient plane source and differential scanning calorimetry techniques were utilized to measure the thermal conductivity and latent heat of the fabricated CPSF/P-FSPCM. The obtained results showed that after increasing the porosity of CPSF/P-FSPCM from 47% to 74%, its thermal conductivity and latent heat changed from 17.18 W/mK and 32.69 kJ/kg to 156.30 W/mK and 11.61 kJ/kg, respectively. Further, the produced CPSF/P-FSPCM possessed the ability to significantly accelerate the heat transfer process and maintain the temperature of a device within a safe range. Finally, a CPSF/P heat sink for high power density light-emitting diodes (LEDs) was fabricated. After 10 on/off testing cycles conducted at a power of 18 W, the temperature of the CPSF/P heat sink varied between 93.7 °C and 57.5 °C, thereby decreasing the highest temperature by 16.3 °C, improving the LED brightness by 4.07% and decreasing its variation by 2.12% as compared to that of conventional aluminum heat sinks. The results presented in this work indicate that the prepared CPSF/P-FSPCM represents a high-potential material for reliable thermal management.

1. Introduction

As modern electronic devices evolve towards smaller sizes, higher power consumption, and larger heat flow densities, their thermal management becomes an important issue. The current market is in urgent need of a stable and effective thermal management technology that can alleviate the temperature increase observed for high-power-density electronic applications such as light-emitting diodes (LEDs), insulated-gate bipolar transistors, batteries, and photovoltaic modules

[1,2]. Phase change materials (PCMs), especially organic solid-liquid ones, exhibit large latent heats (LHs), high chemical stability, and non-toxicity; as a result, they not only demonstrate high robustness that allows the prevention of over-heating in electronics, but can also minimize the size of the utilized thermal management system [3–7].

Variations in the physical state and shape of organic solid-liquid PCMs as well as their low thermal conductivity are the most significant parameters that limit the practical application of these materials [8–11]. Such variations observed before and after the phase change can

* Corresponding author at: 1113 ME Etcheverry Hall, University of California at Berkeley, CA 94720, United States.
E-mail address: ding.xinrui@mail.scut.edu.cn (X. Ding).

<http://dx.doi.org/10.1016/j.apenergy.2017.10.046>

Received 7 June 2017; Received in revised form 11 September 2017; Accepted 6 October 2017
0306-2619/© 2017 Elsevier Ltd. All rights reserved.

produce excessive pressure inside a sealed container. A possible solution to this problem is the use of phase change capsules fabricated from elastic polymers [12,13] to seal the PCM and prevent its leakage. Liu et al. [12] studied the inward solidification heat transfer of the PCMs placed inside spherical capsules by a volume shrinkage method and did not observe any leakage. Fan et al. [13] investigated the heat transfer performance of a PCM-filled circumferentially finned spherical capsule, both experimentally and theoretically. The obtained results showed that the addition of fins decreased the melting duration time by 30% as compared to that of the regular capsules without PCM leakage. Another approach called an organic/inorganic skeleton technology [14,15] uses porous materials as skeleton supporters to retain PCMs. Zeng [14] used myristic acid (MA) as the heat-storing PCM and polyaniline (PANI) as the supporting material to fabricate an MA/PANI form-stable PCM (FSPCM) through a surface polymerization method (here, MA solid particles were completely enclosed by PANI). After all MA species were completely transformed into the liquid state, they remained trapped inside the PANI without any leakage. The results of thermogravimetry (TG) and differential scanning calorimetry (DSC) analyses showed that the produced FSPCM exhibited high LH enthalpy, which reached the value of 150.63 J/g. The studies conducted by Zeng's research group [15,16] showed that the prepared tetradecanol/expanded graphite and palmitic acid/polyaniline/exfoliated graphite FSPCM nanoplatelets did not leak and could be used directly without additional sealing. Cai et al. [17–19] developed a novel FSPCM containing a capric-lauric-palmitic acid eutectic mixture uniformly distributed across the supporting frame fabricated from electrospun SiO₂ nanofibers. The LH of the produced PCM reached a magnitude of 96.5 J/g without leakage after 50 rounds of thermal cycling. Although the use of phase change capsules and organic/inorganic skeletons can successfully resolve the leakage issue, low thermal conductivity of both materials remains a serious problem.

The currently used solutions for mitigating the low thermal conductivity of PCMs include the preparation of composite PCMs from scattered nanoparticles with high-thermal conductivity [20,21], embedding PCMs into porous metallic skeletons or graphite arrays [22,23], and adding cross fins inside PCM capsules [24,25]. In recent years, various materials including Al₂O₃ nanoparticles [21], Fe₃O₄ nanoparticles [26], hexagonal boron nitride nanosheets [27], herringbone-style graphite nanofibers [28], carbon nanotubes [29,30], carbon nanofibers [20,31], and graphene nanoplatelets [30,31] have been reported as potential nano-fillers for the composite PCMs with high thermal conductivity. Tang et al. [32,33] used an ultrasonic-assisted sol-gel method to obtain a polyethylene glycol (PEG)/SiO₂ FSPCM by mixing high-thermal conductivity Al₂O₃ with Cu powder. The results of DSC and thermal conductivity testing showed that the LH enthalpy of PEG/SiO₂-Al₂O₃ was 124 J/g, while the thermal conductivity of the PEG/SiO₂ matrix increased by 34.0% up to 0.398 W/(m·K) after the addition of 3.3 wt% Al₂O₃. The LH enthalpy of PEG/SiO₂-Cu was 112 J/g, and the thermal conductivity of PEG/SiO₂ increased by 38.1% to 0.414 W/(m·K) at a Cu concentration of 2.1 wt%. In addition, TGA tests showed that both materials possessed excellent thermal stability and setting capability. Zou [34] prepared a novel solid-solid phase change composite brick from polyurethane (PU) and pitch-based graphite foam (PGF; here the carbonaceous support was primarily used for mass production and improving the thermal conductivity of the material). The obtained results showed that the thermal conductivity of PU was enhanced to 10.86 W/(m·K) by its encapsulation in PGF, which was 43 times greater than the original value. It was also found that the produced PU/PGF composite could be used for highly efficient electro-to-heat energy conversion and storage with an efficiency as high as 85%. However, the addition of nano-fillers with high thermal conductivity has its own limitations. First, the filler may precipitate after prolonged use. Second, the addition of fillers reduces the viscosity of liquid PCMs, which in turn weakens thermal convection [35]. The thermal conductivity of PCMs can be also improved by using porous metallic skeletons (including metal-fiber-sintered ones) [36,37]. However, the

limited improvement of thermal conductivity is not sufficient for satisfying the continuously increasing heat storage and dissipation requirements of high-power electronics.

In this study, in order to obtain a high latent heat and high thermal conductivity PCM, a copper-powder-sintered frame/paraffin form-stable phase change material (CPSF/P-FSPCM) was prepared by a vacuum perfusion method. The details of the manufacturing process and experimental setup are described in Section 2. In Section 3, the filling rates of the obtained CPSF/P-FSPCMs with different porosities and thicknesses are analyzed, while their thermal conductivity and LH values were measured through transient plane source (TPS) and DSC methods, respectively. Further, the thermal management ability of the prepared CPSF/P-FSPCM was also characterized at different filling rates, porosities, and input powers. Finally, in Section 4, we described the development of a CPSF/P-FSPCM heat sink for cooling high-power LEDs.

2. Materials and methods

2.1. Materials and sample preparation

Dendritic copper powders with five different particle size ranges (550–270 μm, 270–180 μm, 180–150 μm, 150–106 μm, and < 106 μm) were used as the skeleton materials. RT65 paraffin with a melting range of 57–68 °C and solidification range from 67 to 58 °C was selected as the PCM filler.

CPSF/P-FSPCM was fabricated as follows. (1) The copper powders were evenly placed inside high-temperature molds with different thicknesses. (2) The molds were sintered in an HTK8 MO/16-1G vacuum furnace (the protective gas was H₂, and the sintering temperature was 900 °C) for 1 h. (3) Samples S1–S5 were placed in beakers with sufficient amounts of solid PCMs. (4) The beakers were heated to 100 °C for 12 h under vacuum at a background pressure of < 100 Pa to ensure PCM incorporation into the CPSF matrix. Afterwards, the samples were cooled down inside the oven to ambient temperature. (5) Finally, the samples were repeatedly heated and cooled from ambient temperature to 100 °C 10 times to remove unstable PCM species from the CPSF surface (the main parameters of the CPSF samples S1–S5 are listed in Table 1). For each porosity value, eight samples with different thicknesses were fabricated to estimate the PCM filling rate (see Fig. 1). The porosity of CPSFs could not be controlled, but was calculated after sintering using the following equation:

$$\varepsilon (\%) = \left(1 - \frac{M_{\text{CPSF}}}{\rho_{\text{Cu}} V_{\text{CPSF}}} \right) \times 100\% \quad (1)$$

where V_{CPSF} and M_{CPSF} are the volume and mass of the CPSFs, and ρ_{Cu} denotes the density of the copper powder. The cross-sectional scanning electron microscopy (SEM) images of the samples characterized by the highest porosity of 74% (S1) and lowest porosity of 47% (S5) with and without RT65 are shown in Fig. 2, which indicates that the CPSF copper powders are fully covered by the PCM.

2.2. Experimental setup

The utilized temperature measurement system is shown in Fig. 3. It includes a chamber, four K-type thermocouples, a direct current (DC) power source (current: 0–5 A, voltage: 0–210 V), and a data acquisition module with a resolution of 0.1 K. The chamber contains four

Table 1
Properties of the five CPSF samples and their corresponding CPSF/P-FSPCM indices.

Sample	S1	S2	S3	S4	S5
Grain size (μm)	550–270	270–180	180–150	150–106	< 106
Porosity	74%	68%	64%	61%	47%

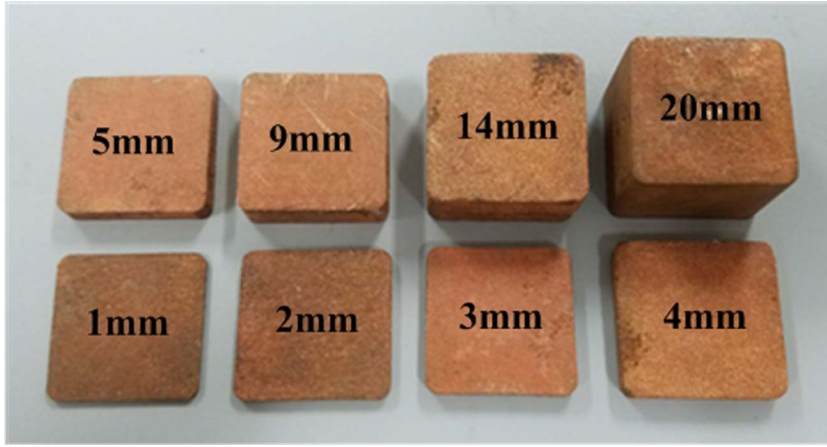


Fig. 1. A photograph of the eight CPSFs with various thicknesses (sample S3 was used as an example).

polymethyl methacrylate and two wooden plates. A film heater with dimensions of $30 \times 30 \times 1.2 \text{ mm}^3$ is in close contact with the CPSF/P-FSPCM composite (the relatively low thermal conductivity of the chamber allows minimization of possible heat losses to ensure sufficient accuracy of the measurements). The locations of the four thermocouples are shown in Fig. 3 as well. Here, T_1 is the temperature at the center of the film heater, T_3 is the temperature at the core of the CPSF/P-FSPCM sample, and T_2 and T_4 are the temperatures measured at distances of +5 mm and -5 mm along the axis of the testing setup, respectively. The uncertainty of the thermocouple readings was within $\pm 0.1 \text{ K}$, while the uncertainty of the DC power output was below 0.1%.

3. Results and discussion

3.1. Basic characteristics

3.1.1. Filling capability

The initial filling rate (IFR) corresponding to the filling rate of PCM in CPSF pores at the beginning of the process, final filling rate (FFR) representing the PCM filling rate after the heating-cooling cycles, initial

mass fraction (IMF) corresponding to the mass fraction of PCM at the beginning of the process, final mass fraction (FMF) equal to the mass fraction of PCM after the heating-cooling cycles, difference in the filling rate (DFR), and difference in the mass fraction (DMF) of CPSF/P-FSPCM were estimated in this work (see Figs. 4 and 5). In particular, the values of IFR and FFR were calculated through Eq. (2), while the IMF and FMF magnitudes were estimated via Eq. (3).

$$I(\%) = \frac{M_{\text{CPSF/P}} - M_{\text{CPSF}}}{\rho_{\text{PCM-s}} \varepsilon V_{\text{CPSF}}} \times 100\% \quad (2)$$

$$\omega(\%) = \frac{M_{\text{CPSF/P}} - M_{\text{CPSF}}}{M_{\text{CPSF/P}}} \times 100\% \quad (3)$$

Here $M_{\text{CPSF/P}}$ is the mass of CPSF/P-FSPCM before and after the heating-cooling cycles, $\rho_{\text{PCM-s}}$ denotes the density of the solid PCM, and ε represents the porosity of CPSF.

When the thickness of the CPSF/P-FSPCM was maintained constant, its IFR, IMF, and FMF increased with increasing porosity. However, the changes in FFR demonstrated the opposite trend, which was caused by the pore tension preventing the permeation of the liquid PCM into the CPSF/P-FSPCM interspace (the pore tension typically increases with a decrease in porosity, leading to a decrease in IFR). Pressure is another

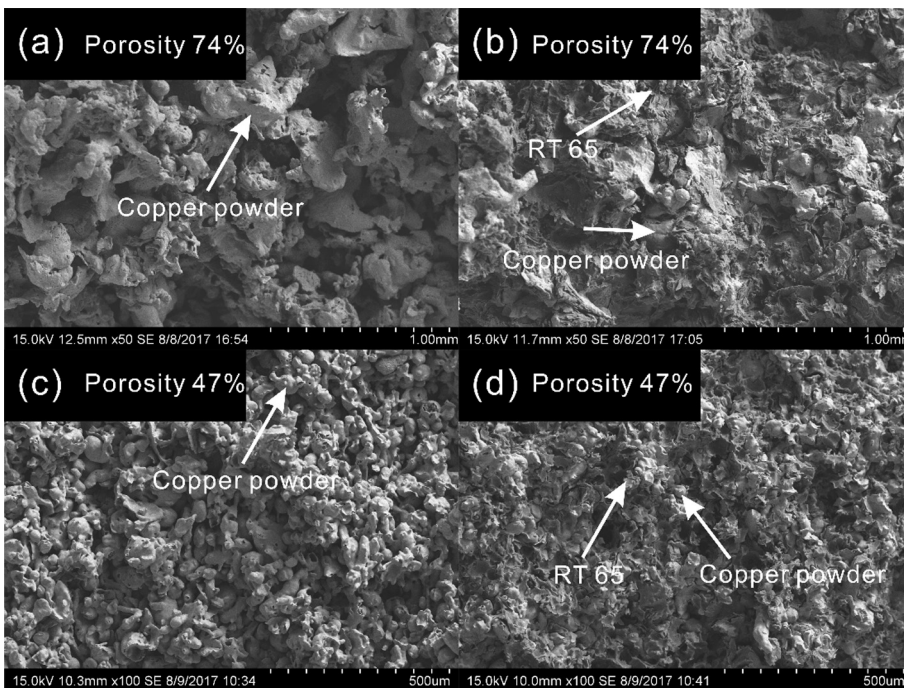


Fig. 2. Cross-sectional SEM images of the samples characterized by the highest porosity of 74% (S1) and lowest porosity of 47% (S5) with and without RT65 filler.

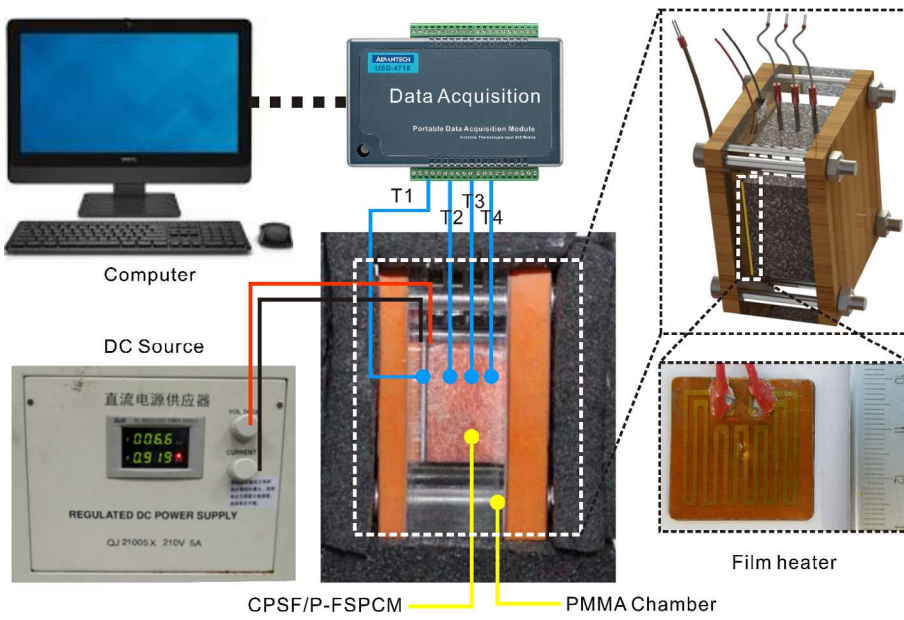


Fig. 3. A schematic describing the testing setup and locations of the thermocouples.

important factor affecting the PCM filling rate. During the filling process, the residual air in the pores act as a barrier preventing the flow of PCM; hence, a vacuum environment is required. Once the CPSF/P-FSPCM is subjected to thermal management under the standard atmospheric conditions after the completion of the PCM filling process, the above-mentioned disadvantages become advantages since they reduce the outflow of the liquid PCM (which explains the almost identical values of FFR obtained for the CPSF/P-FSPCM samples with different

porosities). As the material porosity decreases, the mass fraction of the copper powder increases; as a result, the amount of PCM inside the high-porosity CPSF/P-FSPCM becomes smaller than that inside the low-porosity CPSF/P-FSPCM sample. Therefore, both the IMF and FMF values decrease significantly.

Furthermore, no apparent correlations of IFR and IMF with the thickness of CPSF/P-FSPCM were observed at the same porosities. In contrast, both FFR and FMF vary with the CPSF/P-FSPCM thickness,

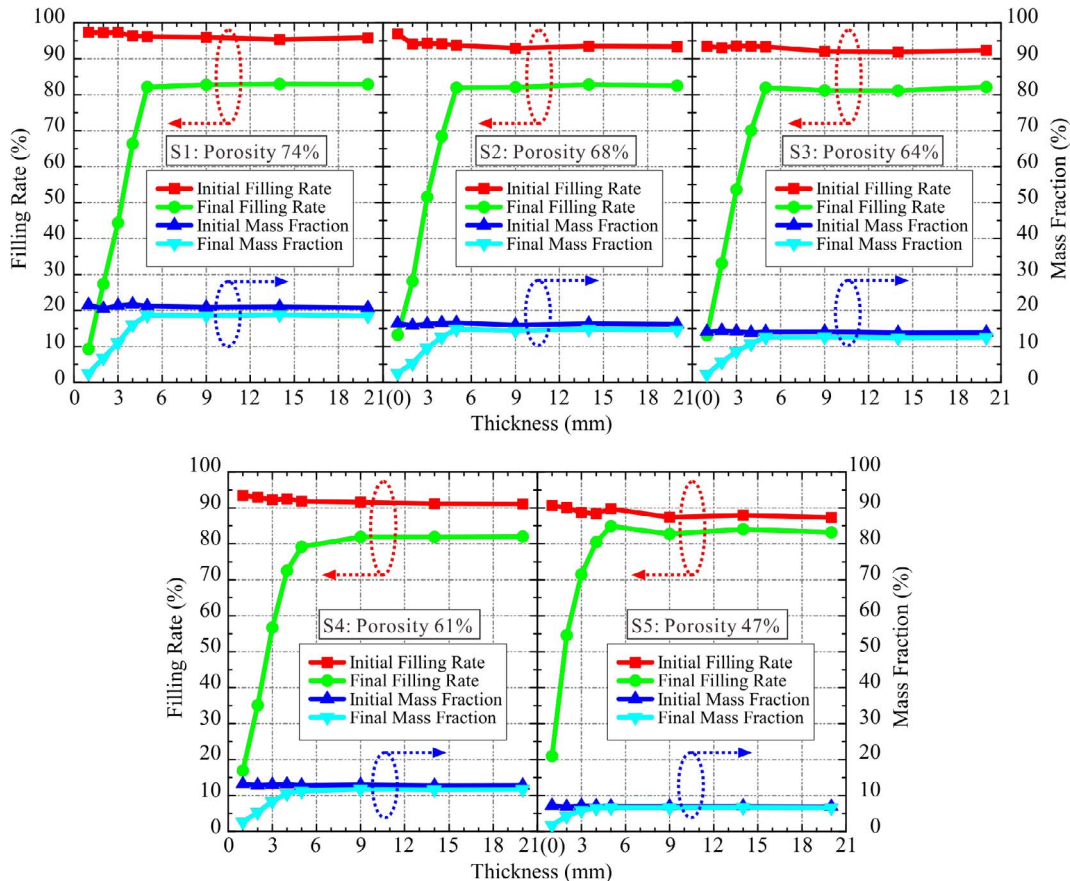


Fig. 4. Dependences of IFR, FFR, IMF, and FMF on the porosity and thickness of CPSF/P-FSPCM.

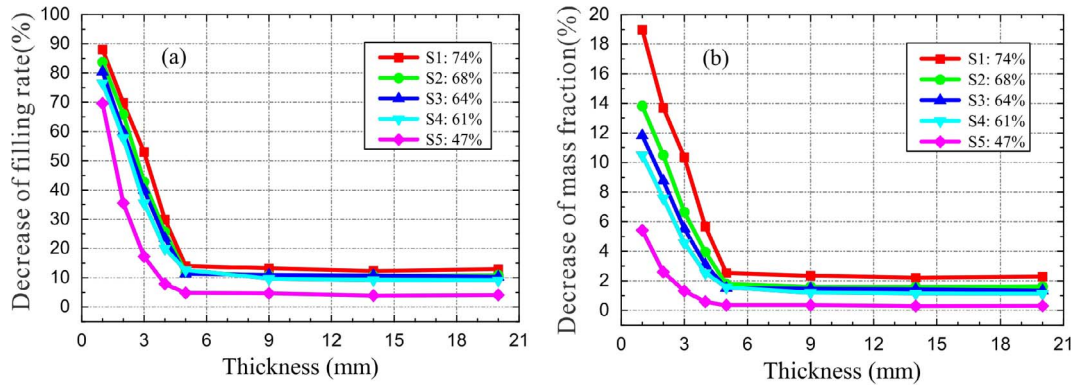


Fig. 5. Dependences of (a) DFR and (b) DMF on the porosity and thickness of CPSF/P-FSPCM.

rapidly increasing in the range from 1 to 5 mm. This phenomenon can be explained by the fact that in the case of an extremely low thickness, the completely open pores of CPSF are unable to retain liquid PCM species. When the CPSF becomes thick enough (between 5 and 20 mm), only a small amount of PCM is removed from its surface, while the majority of PCM species is retained inside the pores; as a result, the magnitudes of FFR and FMF become independent of the CPSF thickness. These variations are consistent with the dependences of DFR and DMF on the porosity and thickness of CPSF/P-FSPCM depicted in Fig. 5.

The cycling stability of CPSF/P-FSPCM is important when the composite is used in real applications. The relative mass losses of the studied five samples were measured before and after a temperature shock, which represented one of the strictest tests in the electronic industry. The temperature cycling procedure started at a temperature of $-40\text{ }^{\circ}\text{C}$ and duration of 30 min. After that, the temperature was increased to $100\text{ }^{\circ}\text{C}$ at a rate of $15\text{ }^{\circ}\text{C}/\text{min}$ and maintained at that level for 30 min. Finally, the temperature was decreased to $-40\text{ }^{\circ}\text{C}$ at a rate of $-15\text{ }^{\circ}\text{C}/\text{min}$ (the entire cycle was repeated 100 times). The resulting mass losses are plotted in Fig. 6, while the inset of this figure describes the details of the temperature cycling experiment. It was found that the high-porosity samples lost a larger amount of the PCM than the low-porosity samples since the latter exhibited stronger pore tensions and thus were able to retain the PCM in the liquid state. Generally, the relative mass losses of all samples were very low. Thus, at the lowest porosity (47%, S5), the relative mass loss was only 0.29%, which confirmed the excellent cycling stability of the prepared CPSF/P-FSPCM. In fact, most of the electronic devices are operated under the temperature conditions (from -20 to $+70\text{ }^{\circ}\text{C}$) that are significantly less harsh than those utilized during the cycling test, indicating that in practical applications, the observed mass losses of CPSF/P-FSPCM

would be even lower.

3.1.2. Thermal properties: Thermal conductivity

A Hotdisk TPS 2500S thermal conductivity analyzer was used to measure the thermal conductivity of the CPSF/P-FSPCM samples with dimensions of $30 \times 30 \times 5\text{ mm}$. Fig. 7 shows that the thermal conductivities of the prepared composites increase with decreasing CPSF porosity, owing to the larger number of thermal transfer paths generated by the sintered necks between the copper particles. For comparison, the thermal conductivities of MA/high-density polyethylene (HDPE) composites containing 8 wt% nano- Al_2O_3 and 12 wt% nanographite were $0.3487\text{ W}/(\text{m}\cdot\text{K})$ and $0.4503\text{ W}/(\text{m}\cdot\text{K})$, respectively [21], while the thermal conductivity of the PEG/boron nitride/graphene nanoplatelets composite PCM was $1.33\text{ W}/(\text{m}\cdot\text{K})$ [38]. The thermal conductivity of FSPCM-CF30 material measured at a temperature of $25\text{ }^{\circ}\text{C}$ was equal to $2.03\text{ W}/(\text{m}\cdot\text{K})$ [39]. In contrast with the results of recent studies [20,23,40,41] that were focused on the enhancement of the thermal properties of FSPCM, the CPSF/P-FSPCMs produced in this work exhibited excellent thermal conductivities ranging from 17.81 to $156.3\text{ W}/(\text{m}\cdot\text{K})$, which were able to significantly improve the application efficiency of PCMs.

3.1.3. Thermal properties: LH enthalpy

In this work, a SETARAM-DSC-131 instrument was utilized to measure the LH enthalpies and phase change temperatures of the studied samples. During experiments, the temperature scanning range was set to $20\text{--}120\text{ }^{\circ}\text{C}$, the heating and cooling rates were equal to $5\text{ }^{\circ}\text{C}/\text{min}$, and the sample mass varied between 5 and 20 mg. The obtained heat flow curves plotted versus the scanning temperature are shown in Fig. 8. Some specific DSC parameters are listed in Table 2. The LH

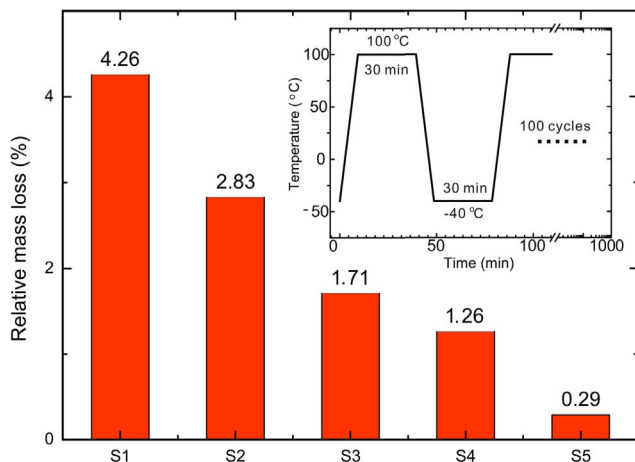


Fig. 6. Relative mass loss of the prepared CPSF/P-FSPCM after temperature cycling.

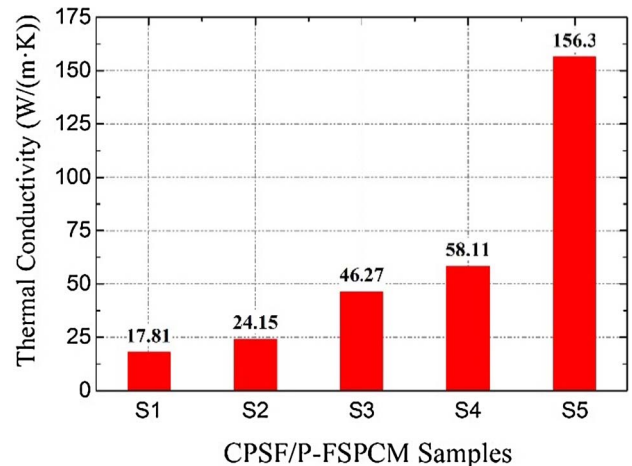


Fig. 7. Thermal conductivities of the CPSF/P-FSPCM samples with different porosities.

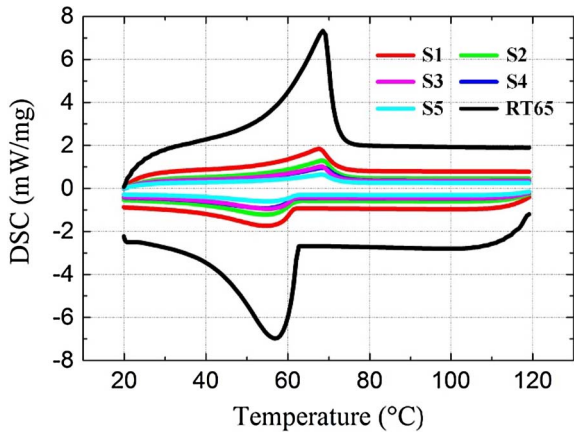


Fig. 8. DSC curves recorded for the five CPSF/P-FSPCM samples with different porosities and RT65 filler.

Table 2

Onset melting points ($T_{m-onset}$), peak melting points (T_{m-peak}), over-melting points (T_{m-over}), measured LH enthalpies (ΔH_m), theoretical LH enthalpies (ΔH_{Tm}), onset solidification temperatures ($T_{s-onset}$), peak solidification temperatures ($T_{s-onset}$), over-solidification temperatures (T_{s-over}), measured LH enthalpies (ΔH_s), and theoretical LH enthalpies (ΔH_{Ts}) of the five CPSF/P-FSPCM samples with different porosities and RT65 filler.

	$T_{m-onset}$ (°C)	T_{m-peak} (°C)	T_{m-over} (°C)	ΔH_m / (kJ/kg)	ΔH_{Tm} / (kJ/kg)	$T_{s-onset}$ (°C)	T_{s-peak} (°C)	T_{s-over} (°C)	ΔH_s / (kJ/kg)	ΔH_{Ts} / (kJ/kg)
RT65	53.1	67.2	70.4	157.2	157.2	62.6	56.9	41.4	157.3	157.3
S1	54.4	67.6	72.2	32.65	31.44	62.1	55.6	40.7	32.69	31.46
S2	54.3	67.9	72.0	24.89	23.58	62.4	55.7	40.1	25.24	23.60
S3	53.9	67.8	72.6	19.65	18.86	62.2	54.8	39.6	19.52	18.88
S4	53.9	68.3	71.5	18.85	18.08	62.4	55.1	39.8	18.73	18.09
S5	54.3	68.0	72.5	11.89	11.31	62.0	55.3	38.9	11.61	11.33

enthalpies of CPSF/P-FSPCM measured during the melting and solidification stages were smaller than that of the pure PCM and decreased with decreasing porosity. Since the skeleton material slightly absorbs heat, the measured LH enthalpies were higher than the corresponding theoretical values. Although the LH enthalpy decreased with increasing thermal conductivity, the phase change LH enthalpy of the fabricated CPSF/P-FSPCM significantly exceeded the values obtained for other materials with similar thermal conductivities. Thus, the thermal conductivity of type 6061 aluminum alloy was 154 W/(m·K); it also exhibited no phase change LH, and its heat capacity was only 896 J/(kg·K). This property of the produced CPSF/P-FSPCM can be used to solve the heat dissipation problem of high-power density electronics.

3.2. Thermal effects observed at different filling modes of CPSF/P-FSPCM

The temperatures (T_1) of the samples of CPSF/P-FSPCM with a porosity of 64%, pure PCM, and CPSF without PCM were measured at different input powers (see Fig. 9). The obtained results show that the magnitude of T_1 increases most rapidly for the sample without PCM, while for the CPSF/P-FSPCM specimen, it demonstrates the lowest increase rate and reaches the smallest value among the studied samples after 80 min. The heating process is mainly affected by the following three factors: thermal conduction, natural convection, and absorption of sensible heat and LH. At an output power of 4 W, the RT65 filler in the pure PCM and CPSF/P-FSPCM samples remains in the solid state without phase change during the initial 20 min, indicating the absence of natural convection. Since the thermal conductivity of CPSF/P-FSPCM is much higher than that of the pure PCM, the heat is transmitted rapidly through the CPSF to RT65, resulting in a slower increase in T_1 . For the pure PCM, a large amount of heat is accumulated on the heating film surface, leading to a rapid increase in T_1 . After 20 min, the value of

$T_{1-CPSF/P-FSPCM}$ is only 62 °C, while $T_{1-Pure PCM}$ is 90 °C, and $T_{1-W/O PCM}$ is 118 °C. During the mid-period (between 20 and 40 min), the CPSF/P-FSPCM system undergoes a phase-changing process; as a result, the observed increase in T_1 slows down significantly. In this region, $T_{1-CPSF/P-FSPCM}$ only increases from 62 °C to 68 °C at a rate of 0.15 °C/min, indicating that the heat was converted to LH by the PCM. During this period, very little convection of CPSF/P-FSPCM was observed since it was limited by the copper powder skeleton. Therefore, the studied CPSF/P-FSPCM specimen mainly exhibited thermal conduction and LH storage (the increase in the T_1 of the pure PCM was smaller during this stage). As the thermal convection became stronger in the liquid PCM, the variations of the rates of increase in $T_{1-Pure PCM}$ and $T_{1-CPSF/P-FSPCM}$ were very close. After this stage, the difference between $T_{1-CPSF/P-FSPCM}$ and $T_{1-Pure PCM}$ reached the largest value of 31 °C. Because the value of $T_{1-W/O PCM}$ quickly approached a heating limit of 120 °C, the input power was switched off at that point to prevent possible device damage. During the final stage (40–80 min), the CPSF/P-FSPCM completed the phase-changing process after 48 min, and its T_1 increased faster than in the previous stage since the natural convection of the liquid PCM remained limited, and the latter could not absorb LH any more. For the pure PCM, the phase-changing process was not complete during this stage, and it continued absorbing LH. The increasing amount of the liquid PCM enhanced the convection transfer process. The increase in T_1 observed between 40 and 80 min was smaller than that occurred during the period between 20 and 40 min. Finally, the values of $T_{1-CPSF/P-FSPCM}$ and $T_{1-Pure PCM}$ reached 88 °C and 103 °C, respectively, and their difference was reduced to 15 °C.

The core temperature (T_3) of the PCM and corresponding temperature difference $\Delta T = |T_1 - T_3|$ are plotted as functions of time in Figs. 10 and 11, respectively. During the first stage (0–20 min), the value of $T_{3-CPSF/P-FSPCM}$ is higher than that of $T_{3-Pure PCM}$ and increases at a faster rate due to the higher thermal conductivity of the CPSF/P-FSPCM sample that efficiently transmits heat through the CPSF and increases the temperature of the PCM core. During the mid-stage (20–40 min), $T_{3-CPSF/P-FSPCM}$ exhibits a significant decrease in the temperature increase rate, which indicates that the sample undergoes the phase change process. On the contrary, the value of $T_{3-Pure PCM}$ increased suddenly in the region of 20–22 min due to the solid-solid phase change. Between 22 and 37 min, no significant differences in the temperature increase rate were observed because only the PCM near the heating film surface experienced a phase change. Between 37 and 40 min, the temperature increase rate increased, indicating that the pure PCM in the center starts to undergo a phase change. During the final stage (40–80 min), the CPSF/P-FSPCM has completed the phase-changing process and stopped absorbing LH. As a result, the magnitude of $T_{3-CPSF/P-FSPCM}$ increased again. For the pure PCM, the temperature increase rate increased faster in the region between 40 and 48 min than during the previous stage. After analyzing the measured temperature values, it can be concluded that in the period between 37 and 48 min, the center of the pure PCM undergoes a phase change. The observed increase in $T_{3-Pure PCM}$ during the phase change stage can be explained as follows. Before melting the center of the PCM specimen, its side adjacent to the heating film has completely melted and accumulated a significant amount of heat. The molten pure PCM exhibits strong natural convection, which promotes a phase change in its central region. The heat absorbed at the location of $T_{3-Pure PCM}$ results not only from thermal conduction, but also from the natural convection of the surrounding liquid PCM. After a larger amount of heat is absorbed, the LH absorbing capacity of the PCM slightly decreases; as a result, the observed temperature increase is accelerated. This explanation is also supported by the data presented in Fig. 11. The value of $\Delta T_{Pure PCM}$ is much larger than that of $\Delta T_{CPSF/P-FSPCM}$, indicating that the presence of CPSF significantly reduces ΔT and makes the application of PCMs more effective.

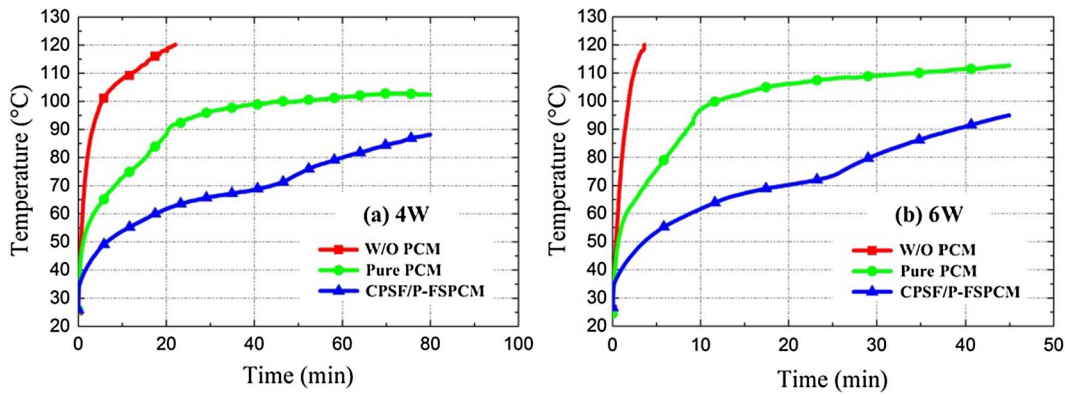


Fig. 9. Curves of T_1 versus time recorded for three filling modes at output powers of (a) 4 W and (b) 6 W.

3.3. Thermal effect of CPSF porosity

Fig. 12 shows the curves of T_1 versus time recorded for the five samples (S1–S5) with various porosities at different input powers. Before the phase change starts, the decrease in the CPSF porosity increases the value of T_1 more rapidly. This phenomenon can be explained as follows. Although lower porosity corresponds to higher conductivity, which promotes the heat transfer to the PCM, it also means a smaller amount of the PCM that is capable of absorbing sensible heat. The large amount of heat increases the PCM temperature T_3 rapidly and reduces the difference between T_3 and T_1 . As a result, the thermal conduction from the heating film to the PCM becomes weaker. The sensible heat absorption plays a more important role at this stage than the thermal conduction process. In the following stage, samples S1 to S5 undergo a phase change, which starts earlier for the samples with low porosity. During this stage, the relatively high value of the LH absorption reduces the increase in the T_1 of all samples. Afterwards, the samples with lower porosities complete the phase change process earlier than the specimens with higher porosities, and their increase in T_1 accelerates until the end of the measurement because the value of T_1 is mainly affected by the thermal conduction, natural convection, and sensible heat absorption after the completion of the phase change process. Although the samples with lower porosities exhibit higher thermal conductivities, they demonstrate more limited natural convection and less sensible heat absorption. Under the combined effect of the three factors, the rate of the temperature increase in later stages is essentially the same for all samples (S1–S5). Since the samples with lower porosities possess higher temperatures before the phase change, they also exhibit higher temperatures after the phase change process. The CPSF/P-FSPCMs with higher CPSF porosities are characterized by longer temperature control times, indicating that these materials can maintain the target temperature at lower values.

Fig. 13 shows the curves of T_3 versus time recorded for samples S1 to S5 with various CPSF porosities at different output powers. As indicated by the obtained results, the samples with lower porosities demonstrate a faster increase in T_3 ; they also undergo a phase change earlier, experience a shorter phase change process, and reach higher temperatures at the end of the testing period. Fig. 14 shows the variation of the temperature difference $\Delta T = |T_1 - T_3|$ with time. After the testing procedure is initiated (0–2 min), the heat has not been transmitted to the PCM yet. As a result, the accumulation of heat on the heating film causes a large instantaneous increase in ΔT from 0 °C to 5.5 °C. Between 2 and 20 min, the heat starts to be transmitted to the PCM, and the magnitude of ΔT decreases significantly. It should be noted that sample S1 exhibited different behavior. Between 5 to 16 min, the value of ΔT_{S1} increased because S1 contained the largest amount of PCM, which underwent a solid-solid phase change under low-power heating (the solid-solid phase change of PCMs increased the absorption of LH; as a result, T_3 increased less rapidly, and ΔT_{S1} increased as well). A similar phenomenon was observed for samples S2 to S5 (see in Fig. 14(a)). However, since the CPSF/P-FSPCM samples with high thermal conductivity and low porosity contain small amounts of PCM, their ΔT remained almost unchanged. The lower is the CPSF porosity, the shorter is stable period of ΔT (thus, the magnitudes of ΔT_{S2} , ΔT_{S3} , ΔT_{S4} , and ΔT_{S5} remain unchanged between 5 and 15 min, 5 and 14 min, 5 and 13 min, and 5 and 10 min, respectively). After 20 min, the phase change of the PCM increases the LH absorption and storage, which leads to an increase in ΔT . After the completion of the phase change process, the T_1 and T_3 of samples S1–S5 resume a faster temperature increase. Meanwhile, the natural convection that occurs in the liquid PCM transfers more heat from the heating film to the PCM; as a result, the value of ΔT decreases. The samples with lower porosities are less affected by the CPSF; thus, they exhibit more intense natural convection and decrease in ΔT .

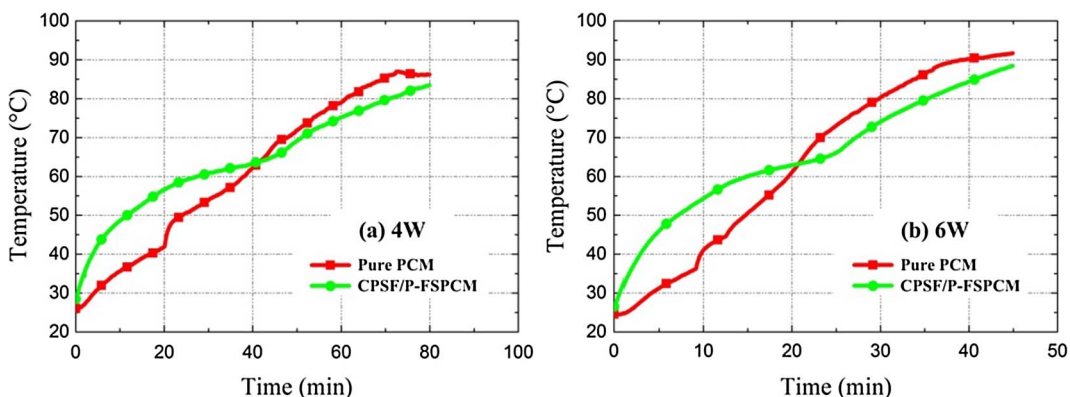


Fig. 10. Curves of the PCM core temperature T_3 versus time recorded for the two filling modes of the studied samples at output powers of (a) 4 W and (b) 6 W.

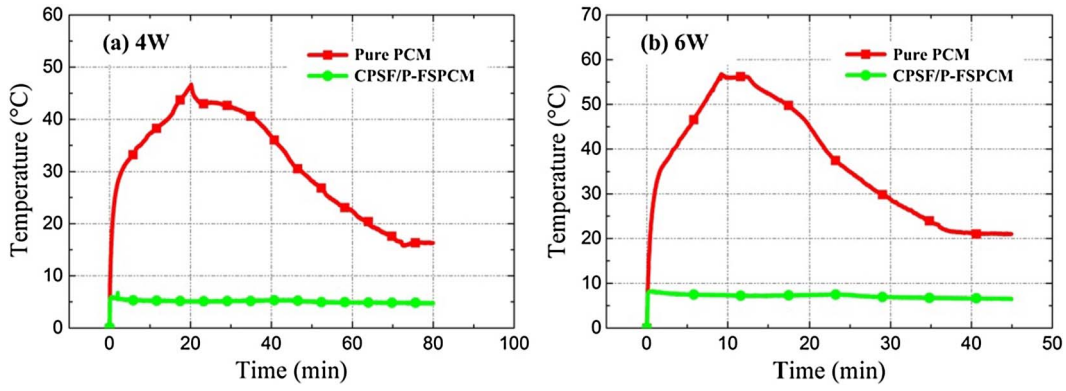


Fig. 11. Temperature differences ΔT measured for the two filling modes of the studied samples at output powers of (a) 4 W and (b) 6 W.

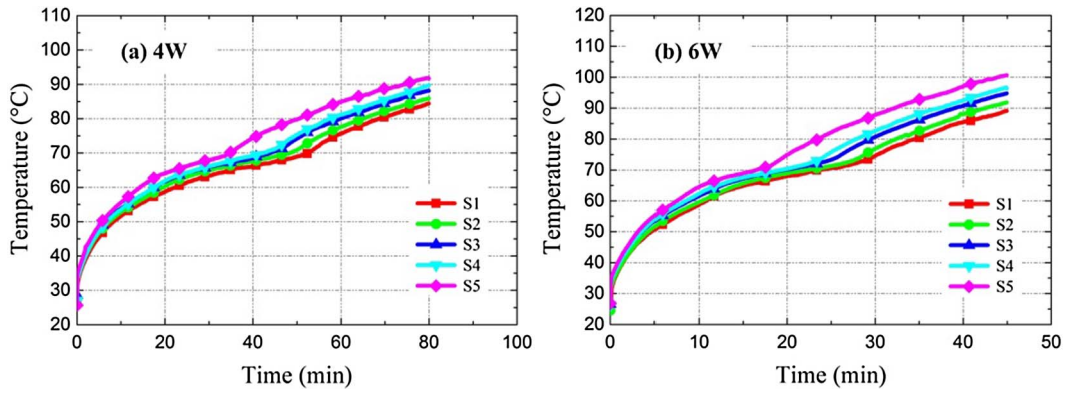


Fig. 12. Curves of T_1 versus time recorded for the five samples with various CPSF porosities at output powers of (a) 4 W and (b) 6 W.

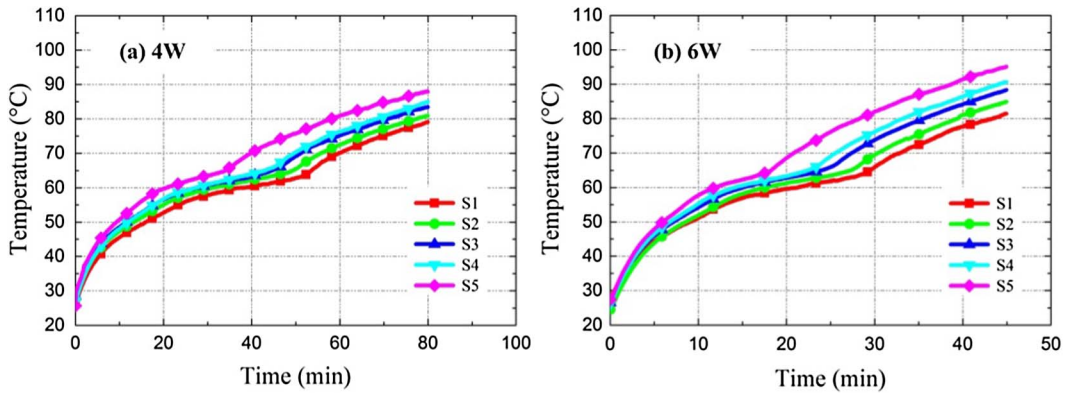


Fig. 13. Curves of T_3 versus time recorded for the five samples with various CPSF porosities at output powers of (a) 4 W and (b) 6 W.

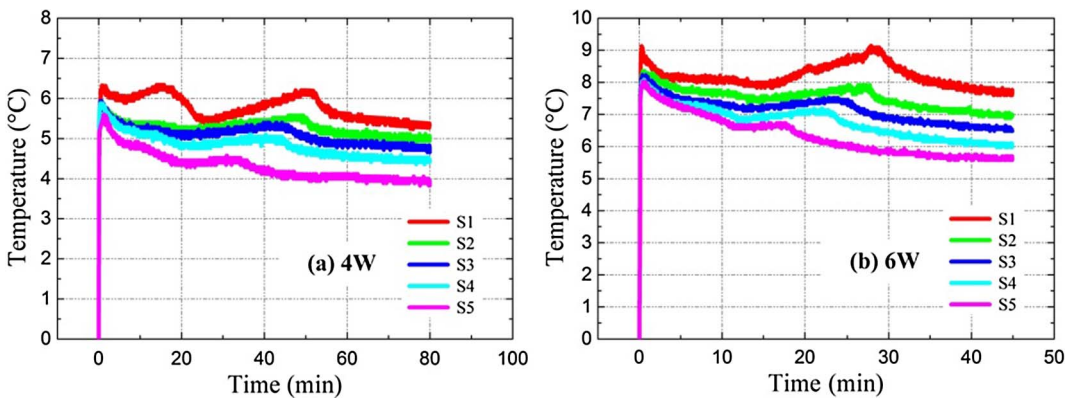


Fig. 14. Temperature differences ΔT measured for the five samples with various CPSF porosities at output powers of (a) 4 W and (b) 6 W.

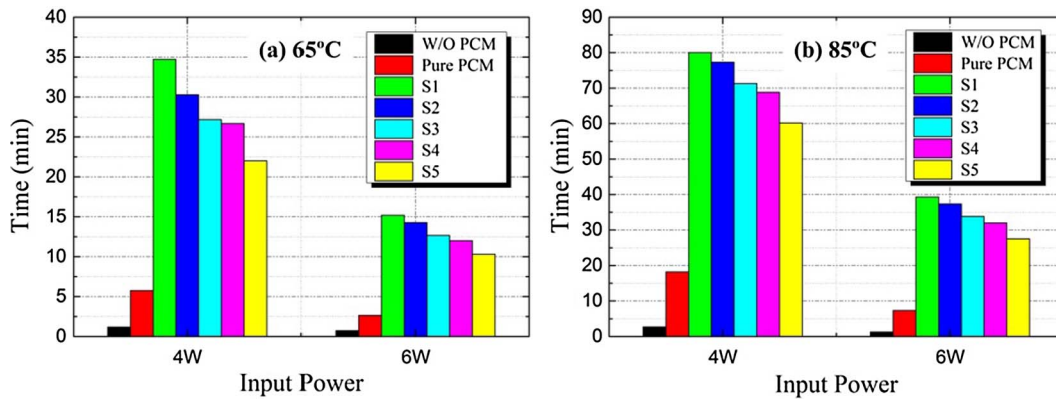


Fig. 15. Times required to reach the critical temperatures of (a) 65 °C and (b) 85 °C.

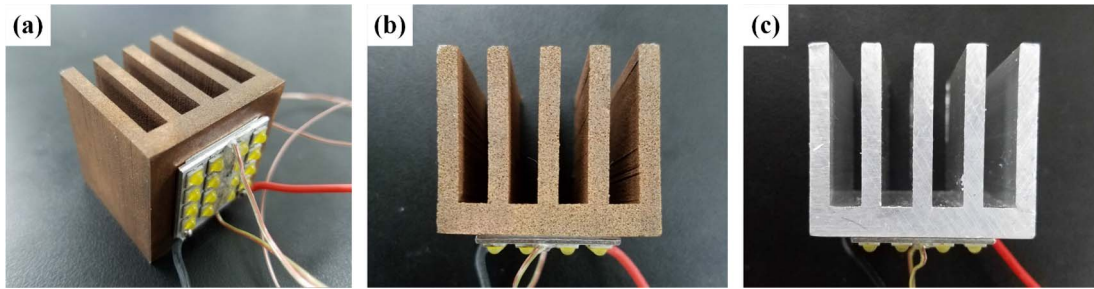


Fig. 16. Photographs of the (a), (b) CPSF/P and (c) aluminum-finned heat sinks.

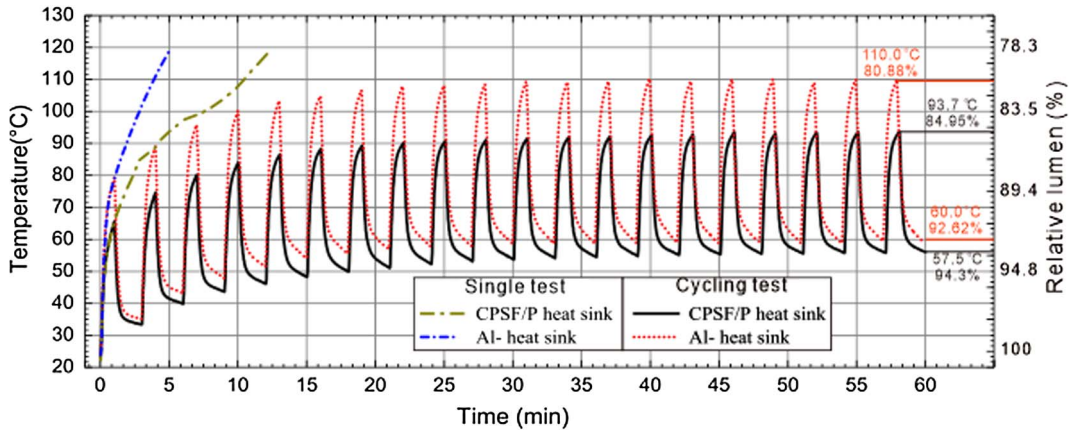


Fig. 17. Temperature curves recorded for the LED devices cooled by the fabricated CPSF/P and aluminum-finned heat sinks.

3.4. Thermal effects on critical duration time

The critical duration time T_{CD} denotes a period, during which a device operates at a certain value of the critical temperature (which usually corresponds to the maximum permitted temperature that allows its continuous operation). In this study, the critical temperatures were 65 °C and 85 °C. Fig. 15 shows a comparison of the critical times obtained for various filling modes and CPSF/P-FSPCM porosities at 65 °C and 85 °C. The value of $T_{CD-W/O\ PCM}$ equal to 2.67 min was the smallest one among the studied samples. After introducing the pure PCM, the magnitude of $T_{CD-Pure\ PCM}$ increased to 18.17 min. Nevertheless, the longest critical time (80 min) was observed for sample S1 (T_{CD-S1}), which exceeded the values of $T_{CD-Pure\ PCM}$ and $T_{CD-W/O\ PCM}$ by factors of 4.40 and 29.96, respectively. Even for the sample with the lowest CPSF porosity (S5), the critical time (T_{CD-S5}) reached a magnitude of 60.17 min, which was 3.31 times greater than $T_{CD-Pure\ PCM}$ and 22.54 times higher than $T_{CD-W/O\ PCM}$. As compared to similar materials, the CPSF/P-FSPCM prepared in this work demonstrated an outstanding

performance. The fin-containing PCM skeleton developed by Mahmoud [24] exhibited the best critical time of 56.7 min at an input power of 5 W. The metal foam PCM designed by Zhao [42] maintained the heat source temperature under 65 °C and 80 °C for 52.2 and 83.3 min, respectively. The sintered metal fiber PCM developed by Li [36] maintained critical temperatures of 65 °C and 90 °C for 17.83 and 35.23 min at a power of 8.54 W, respectively. The performance of the CPSF/P-FSPCM demonstrates that it can be used for improving the thermal management of high-power applications including high-power LEDs, high-performance servers, phased array radars, and artificial satellites. According to the trend depicted in Fig. 15, the value of $T_{CD-CPSF/P-FSPCM}$ decreases with decreasing CPSF porosity at both critical temperatures of 65 °C and 85 °C, which demonstrates that CPSF/P-FSPCM samples with higher porosities allow better temperature control and thus exhibit longer critical operation times.

4. Practical applications

High-power LEDs represent electronic devices characterized by high heat flow density, which experience a serious heat dissipation problem. In order to verify the thermal management ability of the fabricated CPSF/P-FSPCM in practical applications, a heat sink of CPSF/P-FSPCM with a porosity of 68% has been developed for cooling a high-power density LED (see Fig. 16(a) and (b)). The bottom area and thickness of the heat sink were 35×35 mm and 5 mm, respectively, while the number, width, height, and spacing of the fins were 5, 3 mm, 25 mm, and 5 mm, respectively. The LED plate was strongly attached to the bottom of the CPSF/P-FSPCM heat sink using a 3 M thermal conductive adhesive (it consisted of the aluminum baseplate with a size of $20 \times 20 \times 1.5$ mm and 16 FP-3535 WW-BCP-DSR80 LED chips with an input power of 18 W). An aluminum-finned heat sink with parameters identical to those of the CPSF/P-FSPCM heat sink was selected as a control (Fig. 16(c)). Two different testing procedures were performed: a single test at an input power of 18 W (until the LED reached the safety temperature of 120 °C) and 20 on/off cycles (with durations of 1 min and 2 min, respectively). The LED brightness at various temperatures was measured as well.

Fig. 17 shows the temperature curves recorded for the LED devices cooled by the prepared CPSF/P-FSPCM and aluminum-finned heat sinks during the single and cycle tests. The measured temperature corresponded to the average temperature of the two points located at a distance of ± 4 mm from the center of the LED plate. During the single test, the heating rate of the LED plate cooled by the aluminum-finned heat sink was apparently higher than that obtained for the CPSF/P-FSPCM heat sink. After 5.17 min of testing, the temperature of the aluminum heat sink reached the limit of 120 °C. In contrast, after the same period, the temperature of the LED plate cooled by the CPSF/P-FSPCM heat sink was only 94.3 °C, which was 25.7 °C lower than the value obtained for the aluminum-finned heat sink. Upon further heating, the tested LED device reached the temperature limit after 12.57 min, which was 2.43 times greater than the magnitude determined for the aluminum-finned heat sink. After 10 testing cycles, both the aluminum and CPSF/P-FSPCM heat sinks became stable. The highest and lowest temperatures obtained for the aluminum heat sink were 110.0 °C and 60 °C, respectively, while the corresponding values for the CPSF/P-FSPCM heat sink were 93.7 °C and 57.5 °C, respectively. Hence, the use of the CPSF/P-FSPCM heat sink decreased the highest temperature of the aluminum heat sink by 16.3 °C. The obtained results indicate that the temperature difference between the on and off states of the LED (and the corresponding thermal shock) can be significantly reduced by the CPSF/P-FSPCM heat sink, especially in high-power electronics. Moreover, by limiting the thermal shock, the application of the CPSF/P-FSPCM heat sink can also improve the light emission stability of the device. It is well known that the performance of LEDs is very sensitive to temperature, which causes variations in their brightness. The results obtained in this study revealed that the use of the CPSF/P-FSPCM heat sink could increase the LED brightness by 4.07% and reduce its variation by 2.12% as compared with that obtained using the aluminum heat sink. Therefore, the fabricated CPSF/P-FSPCM heat sink can be potentially used for cooling electronic devices with high heat flux densities.

5. Conclusions

In order to mitigate the leakage and low thermal conductivity of commonly used PCMs, a special composite material (CPSF/P-FSPCM) has been developed in this work, and its basic and thermal properties, temperature cycling stability, and thermal management ability were studied experimentally. The observed excellent temperature cycling stability without leakage and high thermal conductivity of CPSF/P-FSPCM make it an ideal candidate for the high-power electronic thermal management. Moreover, the prepared composite can

significantly accelerate the heat transfer process from the heat source to the PCM and thus maintain the heat source at a relatively low temperature and decrease rate of temperature increase. The CPSF/P-FSPCM with a high porosity of the CPSF component contains a large amount of PCM, which is capable of storing more sensible and latent heats; however, its thermal conductivity is very low. In contrast, the low-porosity CPSF/P-FSPCM exhibits relatively high thermal conductivity, indicating that the porosity level of CPSF must be selected depending on a particular application. Finally, a CPSF/P heat sink for cooling a high-power LED has been fabricated; it was able to increase the LED brightness limit by 4.07% and decrease its variation by 2.12% as compared to that of the aluminum heat sink. Thus, the fabricated CPSF/P-FSPCM exhibited high values of both thermal conductivity and LH. The outstanding thermal properties of the studied CPSF/P-FSPCM can enhance its thermal transfer/storage efficiency, which makes it an ideal thermal management material for high-power electronics.

Acknowledgments

This work is supported by the National Natural Science Foundation of China, No. U1401249 and No. 51405161, the Natural Science Foundation of Guangdong Province, No. 2014A030312017, the Science and Technology Program of Guangdong Province, No. 2014B010121002 and No. 2015B010114003.

References

- [1] Sohel Murshed SM, Nieto de Castro CA. A critical review of traditional and emerging techniques and fluids for electronics cooling. *Renew Sustain Energy Rev* 2017;78:821–33.
- [2] Jakhar S, Soni MS, Gakkhar N. Historical and recent development of concentrating photovoltaic cooling technologies. *Renew Sustain Energy Rev* 2016;60:41–59.
- [3] Lin ZY, Zhang ZG, Shi GQ, et al. Review on thermal management systems using phase change materials for electronic components, Li-ion batteries and photovoltaic modules. *Renew Sustain Energy Rev* 2014;31:427–38.
- [4] Rao ZH, Wang QC, Huang CL. Investigation of the thermal performance of phase change material/mini-channel coupled battery thermal management system. *Appl Energy* 2016;164:659–69.
- [5] Kandasamy R, Wang XQ, Mujumdar AS. Application of phase change materials in thermal management of electronics. *Appl Therm Eng* 2007;27(17):2822–32.
- [6] Adeel A, Hafiz MA, Muzaffar A, et al. Thermal performance of phase change material (PCM) based pin-finned heat sinks for electronics devices: effect of pin thickness and PCM volume fraction. *Appl Therm Eng* 2017;112:143–55.
- [7] Jose PC, Philip E. Thermal energy storage for low and medium temperature applications using phase change materials – a review. *Appl Energy* 2016;177:227–38.
- [8] Lv PZ, Liu CZ, Rao ZH. Review on clay mineral-based form-stable phase change materials: preparation, characterization and applications. *Renew Sustain Energy Rev* 2017;68:707–26.
- [9] Yanio EM, Andrea G, Mario G, et al. A review on encapsulation techniques for inorganic phase change materials and the influence on their thermophysical properties. *Renew Sustain Energy Rev* 2017;73:983–99.
- [10] Lv PZ, Liu CZ, Rao ZH. Experiment study on the thermal properties of paraffin/kaolin thermal energy storage form-stable phase change materials. *Appl Energy* 2016;82:475–87.
- [11] Mu ML, Basher PAM, Sha W, et al. Shape stabilised phase change materials based on a high melt viscosity HDPE and paraffin waxes. *Appl Energy* 2016;162:68–82.
- [12] Liu MJ, Fan LW, Zhu JQ, et al. A volume-shrinkage-based method for quantifying the inward solidification heat transfer of a phase change material filled in spherical capsules. *Appl Thermal Eng* 2016;108:1200–5.
- [13] Fan LW, Zhu JQ, Xiao SL, et al. An experimental and numerical investigation of constrained melting heat transfer of a phase change material in a circumferentially finned spherical capsule for thermal energy storage. *Appl Thermal Eng* 2016;100:1063–75.
- [14] Zeng JL, Zhu FR, Yu SB, et al. Myristic acid/polyaniline composites as form stable phase change materials for thermal energy storage. *Sol Energy Mater Solar Cell* 2014;114:136–40.
- [15] Zeng JL, Gan J, Zhu FR, et al. Tetradecanol/expanded graphite composite form-stable phase change material for thermal energy storage. *Sol Energy Mater Solar Cell* 2014;127:122–8.
- [16] Zeng JL, Zheng SH, Yu SB, et al. Preparation and thermal properties of palmitic acid/polyaniline/exfoliated graphite nanosheets form-stable phase change materials. *Appl Energy* 2014;115:603–9.
- [17] Cai YB, Sun GY, Liu MM, et al. Fabrication and characterization of capric-lauric-palmitic acid/electrospun SiO₂ nanofibers composite as form-stable phase change material for thermal energy storage/retrieval. *Sol Energy* 2015;118:87–95.
- [18] Cai YB, Ke HZ, Dong J, et al. Effects of nano-SiO₂ on morphology, thermal energy storage, thermal stability, and combustion properties of electrospun lauric acid/PET

- ultrafine composite fibers as form-stable phase change materials. *Appl Energy* 2011;88:2106–12.
- [19] Cai YB, Hou XB, Wang WW, et al. Effects of SiO₂ nanoparticles on structure and property of form-stable phase change materials made of cellulose acetate phase inversion membrane absorbed with capric-myristic-stearic acid ternary eutectic mixture. *Thermochim Acta* 2017;653:49–58.
- [20] Huang X, Alva G, Liu LK, et al. Microstructure and thermal properties of cetyl alcohol/high density polyethylene composite phase change materials with carbon fiber as shape-stabilized thermal storage materials. *Appl Energy* 2017;200:19–27.
- [21] Tang YJ, Su D, Huang X, et al. Synthesis and thermal properties of the MA/HDPE composites with nano-additives as form-stable PCM with improved thermal conductivity. *Appl Energy* 2016;180:116–29.
- [22] Nomura T, Zhu CY, Nan S, et al. High thermal conductivity phase change composite with a metal-stabilized carbon-fiber network. *Appl Energy* 2016;179:1–6.
- [23] Huang ZW, Gao XN, Xu T, et al. Thermal property measurement and heat storage analysis of LiNO₃/KCl – expanded graphite composite phase change material. *Appl Energy* 2014;115:265–71.
- [24] Mahmoud S, Tang A, Toh C, et al. Experimental investigation of inserts configurations and PCM type on the thermal performance of PCM based heat sinks. *Appl Energy* 2013;112:1349–56.
- [25] Eslamnezhad H, Asghar BR. Enhance heat transfer for phase-change materials in triplex tube heat exchanger with selected arrangements of fins. *Appl Therm Eng* 2017;113:813–21.
- [26] Mahdiah A, Yasaman A, Elaheh SA, et al. Experimental investigation of the effects of using nano/phase change materials (NPCM) as coolant of electronic chipsets, under free and forced convection. *Appl Therm Eng* 2017;111:271–9.
- [27] Fang X, Fan LW, Ding Q, et al. Thermal energy storage performance of paraffin based composite phase change materials filled with hexagonal boron nitride nanosheets. *Energy Convers Manage* 2014;80:103–9.
- [28] Warzoha RJ, Weigand RM, Fleischer AS. Temperature-dependent thermal properties of a paraffin phase change material embedded with herringbone style graphite nanofibers. *Appl Energy* 2015;137:716–25.
- [29] Warzoha RJ, Fleischer AS. Effect of carbon nanotube interfacial geometry on thermal transport in solid-liquid phase change materials. *Appl Energy* 2015;154:271–6.
- [30] Fan LW, Zhu ZQ, Zeng Y, et al. Transient performance of a PCM-based heat sink with high aspect-ratio carbon nanofillers. *Appl Therm Eng* 2015;75:532–40.
- [31] Fan LW, Fang X, Wang X, et al. Effects of various carbon nanofillers on the thermal conductivity and energy storage properties of paraffin-based nanocomposite phase change materials. *Appl Energy* 2013;110:163–72.
- [32] Tang BT, Wu C, Qiu M, et al. PEG/SiO₂-Al₂O₃ hybrid form-stable phase change materials with enhanced thermal conductivity. *Mater Chem Phys* 2014;144:162–7.
- [33] Tang BT, Qiu M, Zhang SF. Thermal conductivity enhancement of PEG/SiO₂ composite PCM by in situ Cu doping. *Sol Energy Mater Sol Cell* 2012;105:242–8.
- [34] Wu WH, Huang XY, Li K, Yao R, Chen R, Zou R. A functional form-stable phase change composite with high efficiency electro-to-thermal energy conversion. *Appl Energy* 2017;190:474–80.
- [35] Parameshwaran R, Deepak K, Saravanan R, Kalaiselvam S. Preparation, thermal and rheological properties of hybrid nanocomposite phase change material for thermal energy storage. *Appl Energy* 2014;115:320–30.
- [36] Wang HF, Wang FX, Li ZT, et al. Experimental investigation on the thermal performance of a heat sink filled with porous metal fiber sintered felt/paraffin composite phase change material. *Appl Energy* 2016;176:221–32.
- [37] Wu YX, Tang Y, Li ZT, et al. Experimental investigation of a PCM-HP heat sink on its thermal performance and anti-thermal-shock capacity for high-power LEDs. *Appl Therm Eng* 2016;108:192–203.
- [38] Yang J, Tang LS, Bao RY, et al. Largely enhanced thermal conductivity of poly (ethylene glycol)/boron nitride composite phase change materials for solar-thermal-electric energy conversion and storage with very low content of graphene nanoplatelets. *Chem Eng J* 2017;315:481–90.
- [39] Tian BQ, Yang WB, Luo LJ, et al. Synergistic enhancement of thermal conductivity for expanded graphite and carbon fiber in paraffin/EVA form-stable phase change materials. *Sol Energy* 2016;127:48–55.
- [40] Zhang XG, Yin ZY, Meng DZ, et al. Shape-stabilized composite phase change materials with high thermal conductivity based on stearic acid and modified expanded vermiculite. *Renew Energy* 2017;112:113–23.
- [41] Nourani M, Hamdami N, Keramat J, et al. Thermal behavior of paraffin-nano-Al₂O₃ stabilized by sodium stearoyl lactylate as a stable phase change material with high thermal conductivity. *Renew Energy* 2016;88:474–82.
- [42] Zhao CY, Lu W, Tian Y. Heat transfer enhancement for thermal energy storage using metal foams embedded within phase change materials (PCMs). *Sol Energy* 2010;84:1402–12.